

Direct Visualization of Irreducible Ferrielectricity in Crystals

Kai Du^{1#}, Lei Guo^{2#}, Jin Peng^{2#}, Xing Chen¹, Zheng-Nan Zhou¹, Yang Zhang², Ting Zheng², Yan-Ping Liang², Jun-Peng Lu², Zhen-Hua Ni², Shan-Shan Wang², Gustaaf Van Tendeloo^{3,4}, Ze Zhang¹, Shuai Dong^{2*}, He Tian^{1*}

¹Center of Electron Microscopy, State Key Laboratory of Silicon Materials, and School of Materials Science and Engineering, Zhejiang University, Hangzhou, 310027, China

²School of Physics, Southeast University, Nanjing 211189, China

³Electron Microscopy for Materials Science (EMAT), University of Antwerp, Groenenborgerlaan 171, B-2020 Antwerp, Belgium

⁴Nanostructure Research Centre (NRC), Wuhan University of Technology, Wuhan, 430070, China

#These authors contribute equally to the work.

*Correspondence to: Email: hetian@zju.edu.cn; sdong@seu.edu.cn;

In solids, charge polarity can one-to-one correspond to spin polarity phenomenologically, e.g. ferroelectricity/ferromagnetism, antiferroelectricity/antiferromagnetism, and even dipole-vortex/magnetic-vortex, but ferrielectricity/ferrimagnetism kept telling a disparate story in microscopic level. Since the definition of a charge dipole involves more than one ion, there may be multiple choices for a dipole unit, which makes most ferrielectric orders equivalent to ferroelectric ones, i.e. this ferrielectricity is not necessary to be a real independent branch of polarity. In this work, by using the spherical aberration-corrected scanning transmission electron microscope, we visualize a nontrivial ferrielectric structural evolution in BaFe₂Se₃, in which the development of two polar sub-lattices is out-of-sync, for which we term it as irreducible ferrielectricity. Such irreducible ferrielectricity leads to a non-monotonic behavior for the temperature-dependent polarization, and even a compensation point in the ordered state. Our finding unambiguously distinguishes ferrielectrics from ferroelectrics in solids.

Introduction

Ferrielectricity, the equivalent of ferrimagnetism, can be termed as antiferroelectric order but with a switchable polarization, as sketched in Fig. 1a. The first proposed ferrielectric system was a composition of two antiferroelectric compounds NaVO_3 and NaNbO_3 [1], but subsequent experiments did not support this claim [2]. Despite a long history, the existence of ferrielectricity in solid crystals remains rare, except in liquid crystals [3]. Recently, some solids were claimed to be ferrielectric. For example, in the layered-structure CuInP_2S_6 , the positions of Cu and In are always opposite within each unit cell (u.c.), which can be recognized as two uncompensated polar sub-lattices with antiparallel alignment [4,5]. In geometric ferroelectrics, such as $\text{Ca}_3\text{Ti}_2\text{O}_7$ and some perovskite superlattices, the displacements of ions are opposite between layers, which can also be recognized as two uncompensated dipole moments [6,7]. Despite the macroscopic and phenomenological analogy as shown in Fig. 1a, it should be noted that there is a key difference between the ferrimagnetic and ferrielectric systems in the microscopic level. Different from the spin moment which can be defined on a single ion, the definition of a charge dipole involves more than one ion and thus may have multiple choices in ionic crystals. By choosing different ions as a dipole unit, multiple dipole values for a sub-lattice can be obtained [8]. In this sense, the Cu-In pair in CuInP_2S_6 or bilayer in $\text{Ca}_3\text{Ti}_2\text{O}_7$ can be treated as a dipole unit, which are indeed entangled simultaneously [4,6]. Therefore, these systems are indistinguishable from ferroelectrics, i.e. ‘reducible’ ferrielectrics, as qualitatively sketched in Fig. 1a. Indeed, CuInP_2S_6 only shows one paraelectric-ferroelectric transition temperature, and in most cases those geometric ferroelectrics are coined as ‘ferroelectrics’ rather than ‘ferrielectrics’ [5,9]. Similar situations also exist for other ferrielectrics like Pb_2MnWO_6 [10]. Conceptually different to these ‘reducible’ ferrielectrics, in this article, we provide proof of an ‘irreducible’ ferrielectricity (see Fig. 1a for its conceptual definition of ‘irreducible’ ferrielectricity) in BaFe_2Se_3 . We will show unique ferri-characteristics clearly distinguishable from ferroelectricity.

Results

BaFe_2Se_3 : ferrielectric material at room temperature

BaFe_2Se_3 belongs to the iron-based superconductor family [11-13] but predicted to be multiferroic under ambient conditions [14]. As shown in Fig. 1b, a BaFe_2Se_3 u.c. contains two

iron ladders (labelled as A and B). Long-range block-type antiferromagnetism (block-AFM) appears below the Néel temperature $T_N \sim 240\text{-}256\text{ K}$ [15-19]. The structural tetramerization due to the block-AFM leads to charge dipoles along the a -axis and the alignment of dipoles is almost antiparallel but with a tiny canting angle ($\sim 5.78^\circ$ at room temperature) between ladders A and B (schematic displacements are shown in Fig. 1c) [14]. It should be noted that all other members of the 123-series iron selenides (e.g. BaFe_2Se_3) also own a similar (quasi-) one-dimensional (1D) ladder structure, but only BaFe_2Se_3 has the canting ladder characteristic. According to theory [14], a residual polarization along the c -axis (P_c) is expected in BaFe_2Se_3 , as a characteristic of a ‘reducible’ ferrielectric material.

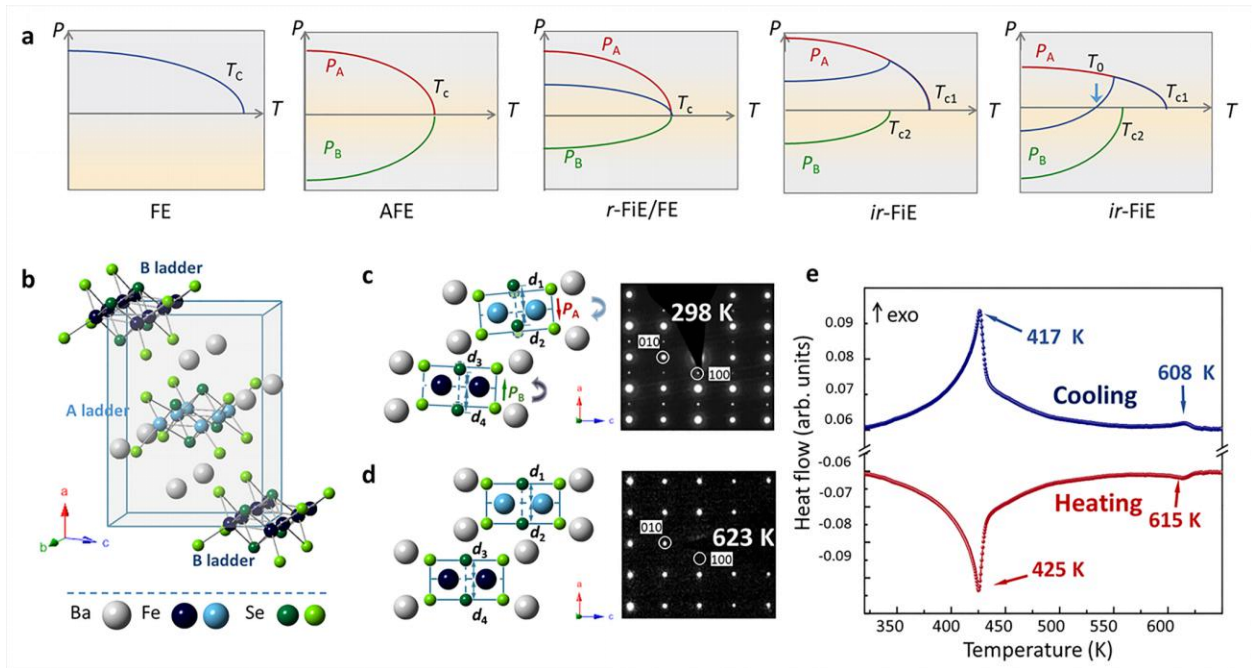


Fig. 1 Concept of ferrielectricity and candidate material BaFe_2Se_3 . **a**, Polarization (P) vs temperature (T) of ferroelectricity (FE), antiferroelectricity (AFE), reducible-ferrielectricity (r -FiE) and irreducible-ferrielectricity (ir -FiE), respectively. In r -FiE, two polar sub-lattices (A & B) develop synchronously, with one unique critical temperature. This type of ferrielectricity is macroscopically equivalent to ferroelectricity. In ir -FiE, the evolution of sub-lattices A & B is out-of-sync, with two critical temperatures (a higher T_{C1} & a lower T_{C2}). A compensation point (T_0) may appear in some ir -FiE systems. Note that any information on the order of the phase transition is not represented in these qualitative cartoons. **b**, Crystal structure of BaFe_2Se_3 . Each unit is composed of two iron-ladders. **c**, Room temperature structure with a tiny tilting

angle between the ladders A and B. **d**, High temperature structure without tilting. The in-situ selected area electron diffraction patterns are shown. The lattice periodicity along the [100] direction changes from 11.90 Å to 5.96 Å as the temperature rises from 298 K to 623 K. **e**, DSC curves indicate two transitions at ~610 K and ~420 K. The ~610 K transition is a second-order one with a step-like behavior, while the ~420 K transition is a first-order one with a peak.

The tilting of the iron ladders gradually disappears with increasing temperature up to ~600 K, leading to a high symmetric *Bbmm* phase, according to X-ray diffraction [16]. Our in-situ selected area electron diffraction (SAED) results give distinctive patterns (Fig. 1c vs Fig. 1d), confirming the disappearance of the ladder canting at high temperature. Differential Scanning Calorimetry (DSC) measurements (Fig. 1e) confirm the phase transition occurring at ~610 K as a second-order one. Besides, there is a first-order phase transition at ~420 K, which was also evidenced in Ref. 16 but its real origin remains a puzzle. In addition, the resistivity behavior also supports this first-order transition (Supplementary Figure 1). Since our neutron powder diffraction (NPD) data confirm that only one block-AFM transition appears at 250 K, obviously, the transition at ~420 K can be excluded as a magnetic-ordering behavior (Supplementary Figure 2a).

Using a spherical aberration-corrected scanning transmission electron microscope (Cs-STEM), we were able to determine the subtle structure evolution of the 1D Fe chains as well as the associated Se's. Then the structure of BaFe₂Se₃ can be directly measured atom column by atom column, which reveals an unexpected irreducible ferrielectricity going beyond the theoretical expectations. The STEM image of BaFe₂Se₃ along *b*-axis and *c*-axis was shown in Supplementary Figure 3. The STEM results at room temperature are summarized in Fig. 2. Interestingly the structural tetramerization already exists at room temperature and, unexpectedly, the intensities for ladders A and B are not equivalent, creating a strong ladder and a weak ladder within a unit cell. The inequivalent features in strong ladders and weak ladders are embodied in magnitude of displacements, as shown schematically in Fig. 2a and in the high-angle annular dark-field scanning transmission electron microscopy (HAADF-STEM) images along the *b* (Fig. 2b and 2d) and *c* axis (Fig. 2c and 2e). The line profiles along these two ladders are shown in Supplementary Figure 4. A displacement vector-mapping algorithm was implemented on the cross-sectional HAADF-STEM images to measure the local displacement of the atoms. Based on the statistics of about 300 data for each length, the Fe atoms displacement in the strong

ladders are stronger than that in the weak ladders (see Supplementary Figure 5 for an example). Considering that the Fe-block tetramerization could induce Se ions displacement along the a -axis [14] (as clearly indicated in Fig. 2b and 2d), such inequivalence of Fe displacements will lead to a residual polarization along the a -axis (P_a), which is larger than the expected P_c . The arrow is added to make it more visible. The uncovered zoom-in images (raw data) have been shown in Fig. 2(b-c). Therefore, BaFe_2Se_3 is a room temperature ferrielectric with polarization mainly along the a -axis, rather than the expected low temperature ferrielectric with polarization along the c -axis [14].

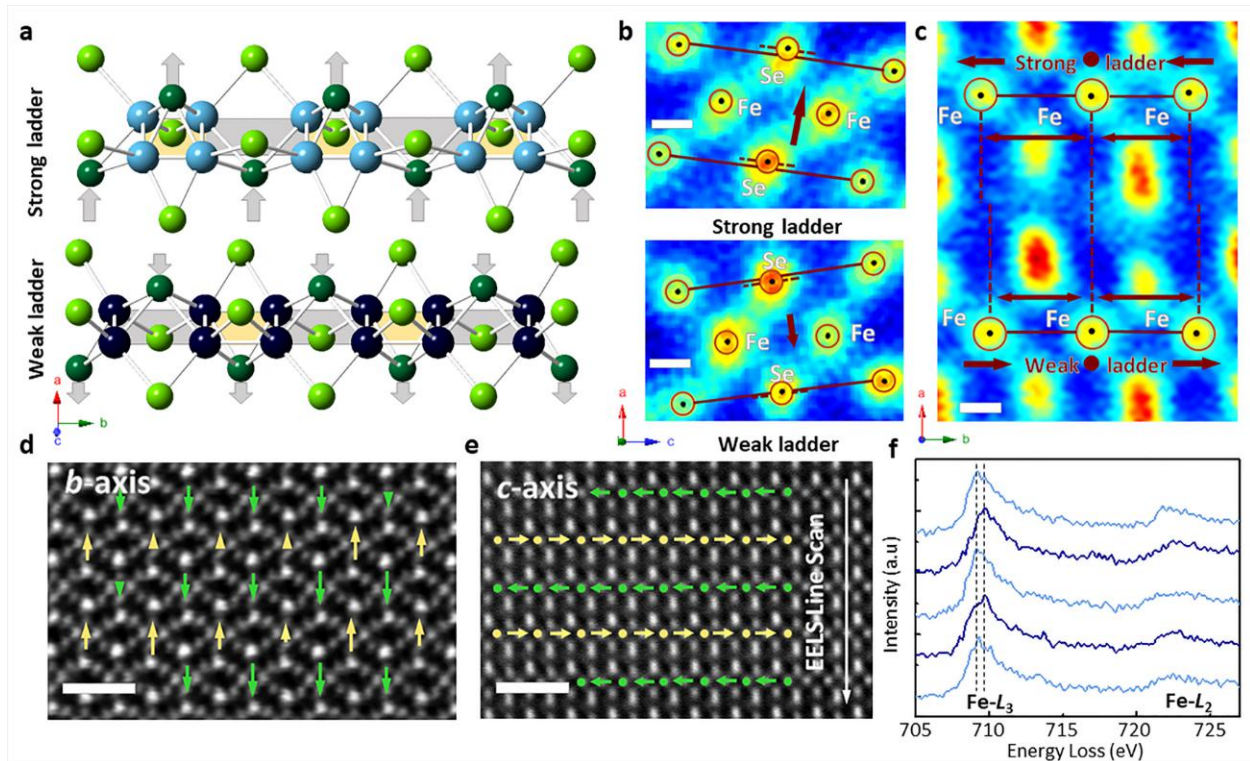


Fig. 2 Atomic displacements in the ladders. **a**, Schematic displacements of Fe and Se ions indicated by arrows and amplified in magnitude. Light blue: strong ladder with larger polar bias of Se ions; Dark blue: weak ladder. **b** and **c**, Color-enhanced HAADF-STEM images of BaFe_2Se_3 along b -axis and c -axis. The strong and weak ladders are distributed in an alternating order. Scale bar, 1 Å. **d** and **e**, Superposition of the HAADF image and the polar map of Se atoms along b -axis and Fe atoms along c -axis. The yellow and green arrows there represent the atoms displacements in strong and weak ladders respectively. Scale bar, 1 nm. **f**, The EELS line scan is across the white line in (e). EELS measurements indicate the charge ordering pattern.

The averaged Fe $L_{2,3}$ edge spectrum from neighboring Fe chains is presented. A Fe- L_3 peak shift of approximately 0.4 eV between neighboring Fe chain is observed.

To explore the origin of this unbalanced ladders, monochromated electron energy loss spectra (mono-EELS) were acquired to demonstrate the underlying charge modulation as shown in Fig. 2f. Using the monochromator we reach an energy resolution of 0.3 eV, which is enough to detect subtle changes in the fine structure of the EELS excitation edges. The averaged Fe- L_3 edges in strong chains and in weak chains show significant differences in their ELNES. Comparing with Fe reference spectra [20], the valence states of the strong and the weak chains in BaFe_2Se_3 are different, and the Fe- L_3 peak shift between them is approximately 0.4 eV (shown as the distance between two dashed line in Fig. 2f). Note that the EELS have an ability to reflect a valance change, but the absolute valance identification is still challenging, since the absolute energy position always has several hundred meV uncertainty. Such charge disproportion is not unusual in correlated electron systems, especially in Fe-based oxides and fluorides, e.g. Fe_3O_4 and LiFe_2F_6 [21, 22], although it has not been reported in selenides before. Nominally, the valences of Fe can become $+(2+\delta)$ and $+(2-\delta)$ for the two sublattices, and a proper δ (around 0.15 according to our fitting results) can lead to the structural tetramerization following the idea of Peierls transition [14]. It should be noted that the non-integer valences are possible in iron selenides, e.g. in KFe_2Se_3 and KFe_2Se_2 [23-25]. Therefore, charge-ordering, i.e. difference of local electron density, can be the key ingredient for the unbalanced structural tetramerization and affiliated polarization, which needs deeper investigation in future.

Variation of the BaFe_2Se_3 structure with various temperature

Then it is interesting to know its ferrielectric T_C . To characterize the structural tetramerization, the difference (δ) of nearest-neighbor Fe-Fe bond length (d) along the ladder direction is measured as a function of temperature (Fig. 3a). An in-situ heating experiment was performed using a DENSSolutions SH30 system to be able to measure over a wide temperature range. A lamella of BaFe_2Se_3 was transferred onto specialized chips using a probe-assistance method (Supplementary Figure 6), then the sample was heated to the set temperature by resistance heating. The displacement vector-mapping algorithm was implemented on the STEM images, and each δ is obtained by averaging around 300 measurements. The difference of Fe-Fe bond length as well as the tilting angle between the ladders at high temperature vanishes ~ 600 K, and the in-ladder tetramerization almost drops to zero, implying a high symmetric nonpolar

phase (in agreement with the DSC curve shown in Fig. 1e and the X-ray data in Ref. [16]). The discrepancy between strong and weak ladders disappears in this high symmetric phase, as also demonstrated by above SAED result (Fig. 1d). With decreasing temperature (e.g. at 473 K), unexpectedly, tetramerization emerges in one sublattice of ladders but not in the other, which is a unique characteristic of irreducible ferrielectricity, leading to an emergence of P_a (Fig. 3b) [calculated by density functional theory (DFT)] [26]. Meanwhile, the ladders become tilting (Fig. 3c compared with Fig. 3d). With further decreasing temperature (e.g. at 423 K), tetramerization emerges in both ladders with different intensities and slopes, implying that the first-order transition occurring at ~ 420 K corresponds to the starting of tetramerization of the weak ladders. At ~ 373 K, the intensities of tetramerization are close to identical between both ladders, resulting in an (almost) canceled P_a , i.e. the unique compensation point (T_0) of irreducible ferrielectricity. Below T_0 , the difference between the two ladders increases with decreasing temperature, leading to a reentrance of P_a . It is worth to emphasize that the direction of polarization (i.e. the roles of strong and weak ladders) may be probably reversed across T_0 according the tendency (see the last panel of Fig. 1a), although our variable temperature measurements can not continuously track the evolution of individual ladder over so large temperature range. If so, the strong ladder A (weak ladder B) becomes the weak ladder A (strong ladder B) when temperature crossing T_0 . More color-enhanced HAADF-STEM images acquired at different temperatures along the c -axis are shown in Supplementary Figure 7. Statistics of the deviation of Fe-Fe bond length in the strong and weak chain at different temperatures could be seen in Supplementary Table 1.

Since the ferrielectric polarization can not be directly measured using electrical methods (and even pizeoelectric force microscopy) in the current stage due to the high leakage of the samples (considering the very small band gap ~ 0.13 - 0.178 eV [17, 18]), an optical second harmonic generation (SHG) experiment is employed to characterize the polarity of the materials (see Methods for experimental details). Our SHG signal (Fig. 3b) demonstrates its polarity below ~ 600 K. Most importantly, the non-monotonic evolution of the SHG signal unambiguously matches the DFT calculated polarization, including the possible compensation point at ~ 380 - 400 K, which provides a very strong evidence to support our STEM data.

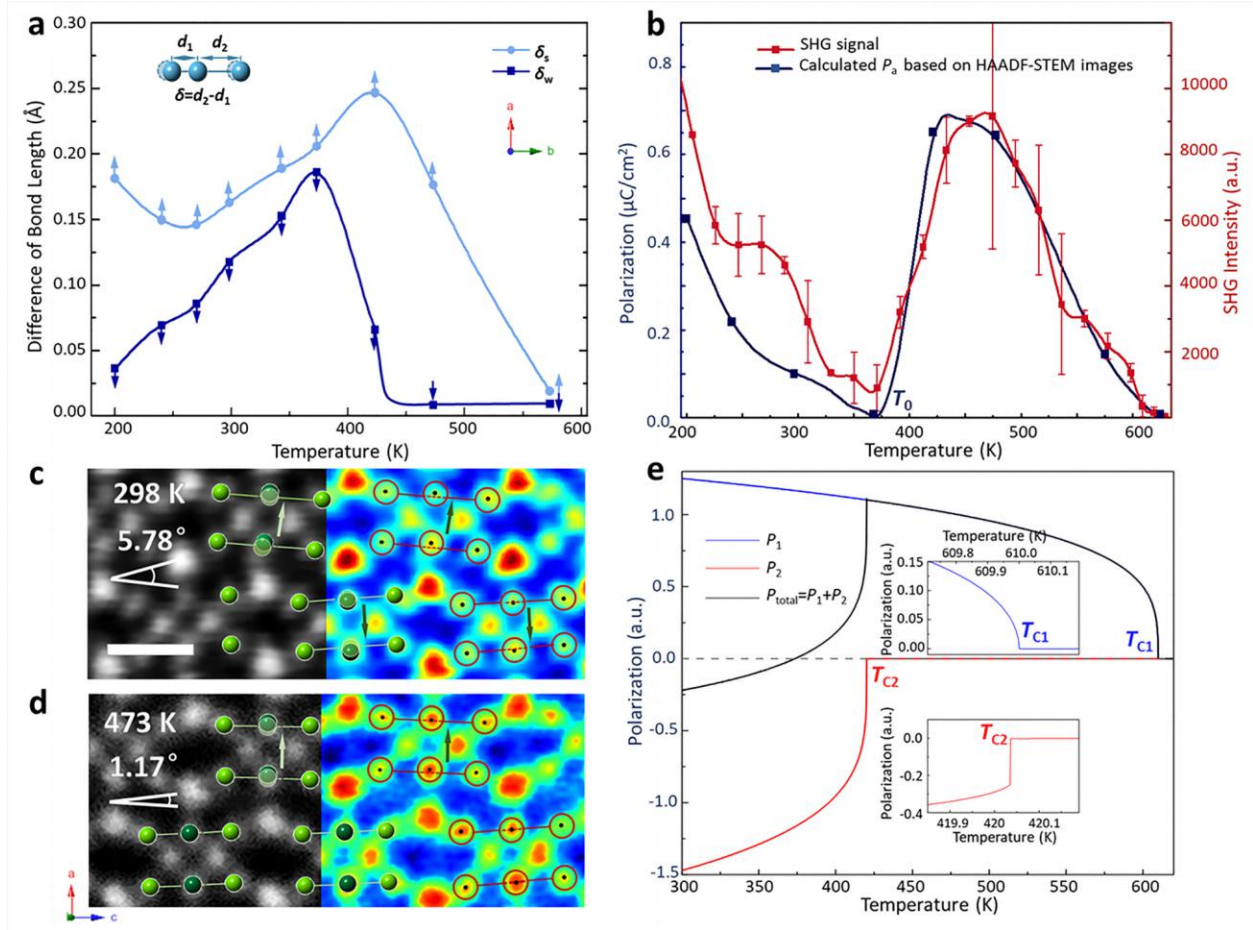


Fig. 3 Temperature-dependent evolution of BaFe₂Se₃. **a**, The measured structural tetramerization. The light blue and dark blue lines correspond to the strong and weak ladders respectively. The affiliated arrows denote the corresponding dipoles. **b**, Left axis: the polarization along the a -axis (DFT calculated using the STEM structural data). Right axis: the SHG signal, which mainly reflects the evolution of P_a . The overall evolutions of the polarization and SHG signal qualitatively match. More SHG data and explanation can be found in Supplementary Figure 8 and Figure 10. **c** and **d**, Color-enhanced HAADF-STEM images acquired at 298 K and 473 K along the b -axis. The Se atoms displacement in the strong chain is larger than that in the weak chain at 298 K; this is consistent with the difference of the Fe chain evolution magnitude at 298 K. Also, the tilt angle between ladders varies from 5.78° to 1.17° at high temperature. Scale bar, 5 Å. **e**, Simulated evolution of order parameters with a most simplified Landau-type free energy formula. Inserts: the magnified views near the phase transitions, which indicate a second-order transition at T_{C1} and a first-order transition at T_{C2} .

The irreducible ferrielectricity of BaFe_2Se_3 can be qualitatively described by Landau theory with a coupling between two ladders (P_A & P_B). The most simplified free energy formula can be written as:

$$F = \alpha_A(T - T_A)P_A^2 + \beta_A P_A^4 + \gamma_A P_A^6 + \alpha_B(T - T_B)P_B^2 + \beta_B P_B^4 + \gamma_B P_B^6 + \alpha_{AB}P_A \cdot P_B, \quad (1)$$

where the first to six items are the standard Landau-Ginzburg-Devonshire type energy expression up to the sixth power for sub-lattices A and B, while the last item is the antiferroelectric coupling between two sub-lattices. All coefficients except β_2 are positive and the small canting angle between P_A and P_B is neglected. Without fine tuning of the coefficients (see Methods for details), the simulated evolution of the polarization (Fig. 3e) is qualitatively reproducing the non-monotonic experimental behavior, implying the correct main physics captured in the model. Consistent with the DSC data, the high temperature transition is a second-order one, while the low temperature transition is a first-order one due to the negative β_2 .

Manipulation of BaFe_2Se_3 by an external electric field

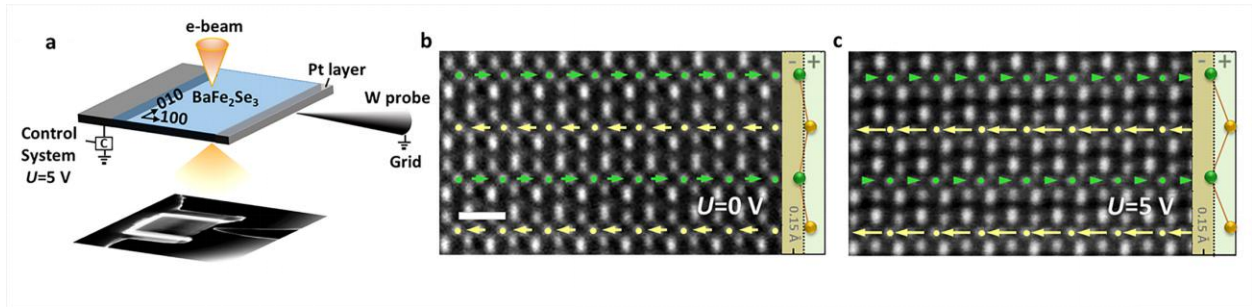


Fig. 4 Manipulation of the ferrielectric polarization in BaFe_2Se_3 . **a**, Schematic diagram of the electric field experiment. The in-situ biasing experiment was performed with an input voltage $V_{\text{DC}}=5$ V. To capture the structural changes, a real-time analysis is performed in STEM mode. **b** and **c**, Comparison of the local dipoles with/without applied voltage. The arrows denote the displacements of 50% of the Fe ions, while the rest of the Fe ions are treated as reference points. The difference between the strong/weak ladders is further enhanced by the electric field. Arrows are added to make the displacements more visible. The uncovered zoom-in image (raw data) can be found in Fig. S9. Scale bar, 5 Å.

As a polar material, electric field tuning of the polarization is a fundamental function. However a direct measurement of the electric hysteresis loop is technically challenging in the current stage due to serious leakage, but we have successfully developed an inspiring in-situ technique to manipulate the polar structure at an atomic scale by applying an electric field. An electrical bias was applied between a tungsten tip, which acts as a mobile electrode, and the lamella of BaFe₂Se₃, which is connected to ground (as schematically shown in Fig. 4a). To capture the changing of atoms positions, the real-time crystal structure with atomic-scale spatial resolution was characterized in STEM mode; the access to dynamic structural information provide a clear picture of the evolution under an external electric field. As shown in Fig. 4b-c and Supplementary Figure 9, the tetramerization is significantly enhanced by applying an electric field along the *a*-axis. This implies a significant enhancement of polarization under the electric field. However, the reversal of P_a has not been achieved, implying a large coercive field.

Previous experiments reported the space group *Pnma* for BaFe₂Se₃ at room temperature [15-17], which is nonpolar and does not allow the tetramerization. A recent work reported the space group *Pmn2₁* (a subgroup of *Pnma*) at room temperature, allowing the tetramerization and polarization [27]. Another recent X-ray diffraction work reported the space group *Pmn2₁* at 300 K but *Pm* (a subgroup of *Pmn2₁* allowing the inequivalent ladders) at 150 K [28]. In fact, the patterns of NPD (or X-ray) are very subtle among these space groups (see Supplementary Figure. 10 and Supplementary Figure11), which thus can not distinguish these structures precisely. Instead, our STEM technique is more suitable to monitor these subtle distortions of inner coordinates. According to our studies, below T_{C1} the accurate space group should already be *Pm*, allowing the asymmetry between two ladders. The transition from *Bbmm* to *Pm* at T_{C1} is a second-order one while the first-order transition at T_{C2} does not change the symmetry. Other high-resolution technique, such as synchrotron X-ray diffraction, may be helpful to verify our STEM results in future.

Discussion

Finally, it should be noted that the irreducible ferrielectrics is not limited to BaFe₂Se₃ but with broader interests. For example, as an important branch of multiferroics, TbMn₂O₅ and other 125-type manganites showed strange ‘ferroelectric’ behavior of polarization as a function of temperature or magnetic field [29,30], including the compensation point of polarization. The

real mechanism is that the ferroelectric contributions in TbMn_2O_5 are from three out-of-sync sources according to the SHG measurement [30].

Even though, our current work on BaFe_2Se_3 is not a marginal extension of TbMn_2O_5 . The polarity in TbMn_2O_5 is magnetism-driven, i.e. it is a so-called type-II multiferroic material, instead of a proper ferroelectric material. It is not rare for a magnetic system to have sequential magnetic phase transitions. In this sense, the nontrivial evolution of polarization in TbMn_2O_5 is just a secondary effect of magnetic evolution, which occurs at very low temperature (<40 K) and gives a very weak signal of polarization ($\sim 0.04 \mu\text{C}/\text{cm}^2$ and $\sim 0.15 \mu\text{C}/\text{cm}^2$) [29, 30]. In our case, the ferrielectricity is not magnetism-driven but a primary polar property, which occurs above room-temperature (15 times of TbMn_2O_5) and with a much larger polarization (5-15 times of TbMn_2O_5). In addition, limited by its very weak polarization signal, the experimental measurements of TbMn_2O_5 can only rely on the pyroelectric method, which can lead to a net polarization but the microscopic facts of different contributions were mostly by suspecting or indirect derivation from SHG signals. Instead, our current work, powered by the advanced in-situ STEM techniques and thanks to the strong signal of BaFe_2Se_3 , the microscopic evolution of two contributions can be visualized directly, leading to a more decisive conclusion. In fact, although the nontrivial polarization of TbMn_2O_5 has been known for decades, it is more likely to be recognized as a type-II multiferroics with strange ferroelectric behavior. Our work will lead to a re-look at the irreducible ferrielectricity, including that in TbMn_2O_5 .

The irreducible ferrielectricity combines both characteristics of ferroelectricity and antiferroelectricity, making these systems having more degrees of freedom to be controlled. For example, by tuning the amplitudes of sub-lattice polarizations near the compensation point, the macroscopic polarization can be easily switched, without the reversal process of dipole moments as required in ferroelectric cases. Moreover, complex ferroelectric+antiferroelectric domain structures may be expected in ferrielectrics [31], which deserve further studies.

In summary, employing spherical aberration-corrected STEM with sub-angstrom resolution, the structural evolution of BaFe_2Se_3 has been characterized in detail. Highly interesting phenomena, beyond previous experimental observations and theoretical predictions, have been detected and analyzed. First, BaFe_2Se_3 is a room temperature polar material. Second, combined with EELS analysis, the origin of its structural tetramerization is demonstrated to be driven by the local electron density, not the previously expected block-type antiferromagnetism. Third,

most importantly, the evolution of the two ladders in BaFe₂Se₃ does not behave synchronously, leading to irreducible ferrielectricity. The compensation point, a unique fingerprint of irreducible ferrielectricity, is observed. The irreducible ferrielectricity reported here is conceptually different from previously reported reducible ferrielectricity which is actually equal to ferroelectricity. The irreducible ferrielectricity in BaFe₂Se₃ acts as the primary effect, leading to a stronger impact to the community to re-investigate this independent branch of polarity. More functionalities are promisingly expected in future based on irreducible ferrielectricity, e.g. the magnetic-field-tunable polarization as demonstrated in TbMn₂O₅.

Methods

Material synthesis. High-quality BaFe₂Se₃ single crystals were grown by the self-flux technique starting from an intimate mixture of Ba pieces, Fe granules, and Se powders with an atomic ratio of 1: 2 : 3. Then the starting materials were put in a carbon crucible and sealed in the quartz tube with partial pressure of argon. The quartz tube was first heated to 420°C at a rate of 1 °C/min, held for 12 h, and then annealed at 1150 °C for another 24 h. After that, the quartz tube was slowly cooled down to 750 °C at a rate of 3°C/h. Finally, the quartz tube was cooled down to room temperature naturally and the strip-like BaFe₂Se₃ single crystals with a typical size of 3.0× 1.0 × 0.5 mm³ and shiny surfaces can be obtained.

Macroscopic properties measurements. Differential scanning calorimetry (DSC) experiments were performed with Maia DSC 200 F3. Measurements were performed on heating and cooling with a rate of 10 K·min⁻¹. The sample is encapsulated in a standard Al crucible using argon stream as the protecting gas. XRD measurements were performed on Rigaku Smartlab3 with Cu *K*_α radiation. In the SHG measurements, the incident laser with a wave length of 800 nm is perpendicular to the cleavage (100) plane and the reflected light at 400 nm is collected. The polarization of the incident laser is controlled by a half wavelength plate. Then the canting polarization along the *c*-axis can be monitored, which is in proportional to the main component of polarization along the *a*-axis. The SHG signal in Fig. 3b was measured with the polarization of the incident laser (i.e. the electric field component *E*) in the *bc* cleavage surface (Fig. S10c) of the BaFe₂Se₃ crystal, while the angular-dependent results with rotating *E* can be found in Fig. S8. Magnetic measurements were carried out in a vibrating sample magnetometer (VSM)

integrated in a Physical Property Measurement System (PPMS-9, Quantum Design) up to 600 K. Neutron Powder Diffraction (NPD) data were collected on a High-intensity Powder Diffractometer Wombat at Australian Nuclear Science and Technology Organization (ANSTO) with $\lambda=2.41$ Å, between 10 K and 500 K. Resistivity was measured using Keithley 4200A-5CS.

Conventional and scanning transmission electron microscopy. Samples was cut into lamellas by Focused Ion Beam (FEI Quanta 3D FEG) for the observation of electron microscope. We use spherical aberration correction electron microscopy (FEI Titan G2 80-200 ChemiSTEM, 30 mrad convergence angle, 0.8 Å spatial resolution) to acquire atomic resolution HAADF-STEM images of BaFe₂Se₃'s cross section from different directions and the image noise was corrected using Digital Micrograph. All STEM images in this work are filtered in Fourier space using a grid mask to select for the lattice frequencies and by low and high pass annular filters to remove the zero frequency and high frequency noise above the information transfer limit. Electron Energy Loss Spectroscopy (EELS) test was also performed on BaFe₂Se₃ to verify whether there are changes in the valence state of iron. SAED patterns (selected area electron diffraction) obtained on FEI Tecnai G2 F20 S-TWIN are used to verify the analysis on the local evolution in the statistical sense. Some additional details should be mentioned: 1) As to exclude the influence of microscope artifacts, some steps have been taken. To minimize the influence of sample drift, most of the microscopy data for quantitative analysis are acquired under the condition of drift below 1 Å min⁻¹. 2) The STEM image were acquired from the mutually perpendicular directions, and the analysis results of bond length show no obvious difference between them. Thus, the possibility of STEM scanning direction as the main origination of the observed phenomenon can be excluded. 3) High frequency vibration of imaging would be another potential influence factor. Therefore, a technique of ultra-fast acquirement was employed. Tens of images were quickly acquired in the same local region, and most HAADF images shown in this article are overlaid based on such image series, the effect of the specimen drift and beam vibration were significantly reduced and the signal-to-noise ratio of the HAADF images was improved, simultaneously. (4) Aiming at avoiding oxidation, experiments were performed as soon as BaFe₂Se₃ was taken out of glove box which offer protecting gas. (5) In consideration of that potential slight damage caused by ion beam in FIB, we minished parameters including voltage and electric current of ion beam down to 2 kV/27 pA to minimize the negative and unnecessary surface damage. For BaFe₂Se₃, the antiferromagnetic ordering temperature is 250 K (Supplementary Figure 2), while most of STEM data are

measured far above this temperature. Thus, the magnetic fields (from Cs-STEM) effect to polar distortion is negligible in the high temperature paramagnetic region.

In-situ study. The in-situ heating experiment was done on DENS solutions SH30 system in order to carry out the experiment in a wide temperature range. The Nano-Chip we used could control the temperature environment locally on the device via the 4-point-probe. Its highest temperature accuracy and stability is 0.001 °C. The experimental data at low temperature was obtained by a demo low-temperature sample holder made by DENS. The in-situ biasing was done on Hysitron PI-95 TEM PicoIndenter, the input voltage $V_{DC}=5$ V was applied between the sharp conductive tip and the sample using a function generator. To capture the changing of atoms positions, the real-time crystal structure is characterized in STEM. The atomic-scale spatial resolution of STEM and the access to structural information provide a clear picture of the evolution under external electric field.

Specimen transfer onto biasing chips. To measure the performance of $BaFe_2Se_3$, as shown in Supplementary Figure 6. After conventional FIB process of welding the lamella onto needle and transfer it near the surface of chips, additional confined Pt pad was deposited to contact the lamella onto the chip surface. The lamella thickness was to about 2 μm . Low current down to 10 pA was used to polish the surface of chips after detaching the needle to reduce the amount of redeposited material resulting from the previous contacting process.

DFT calculation. The DFT calculation was performed based on the projector augmented-wave (PAW) potentials and Perdew-Burke-Ernzerhof exchange function as implemented in Vienna *ab initio* simulation package (VASP) [32-34]. The plane-wave energy was 500 eV. The experimental structures at different temperatures were used and the Cx-type antiferromagnetism is adopted for simplify (since here the polarization is not driven by magnetism). Brillouin zone integration was obtained using a $6\times 3\times 4$ k -point mesh. The standard Berry phase method is adopted to estimate the ferroelectric polarization [35], while the intuitive point-charge-model provides similar results.

Laudau-Ginzburg-Devonshire model. To fit the experimental phase transitions, $T_A=610$ K & $T_B=420$ K, are used. Noting $T_{C1}=T_A$ for the second order phase transition, and T_{C2} is close but slightly higher than T_B for the first order transition. To simulate Fig. 3e, $\alpha_1=1$ as the unit, and $\beta_1=5$, $\alpha_2=4.5$, $\beta_2=-5$, $\gamma_1=\gamma_2=40$. The negative β_2 is essential for the first-order transition around

T_{C2} and the differences between α_1/α_2 , β_1/β_2 originate from the charge disproportion. α_{12} can be a small quantity, e.g. 0.001.

Determining the position of atoms. Polarization mapping here was performed by calculating ion displacements in HAADF-STEM images. On account of the fact that the bright area of every atom in HAADF image is actually too large for us to determine where the center of atom is, a mathematical method involving Gaussian Fitting based on Matlab is essential to ascertain the accurate position of every atom. Gaussian Fitting could give an accurate position of atom according to the brightness of every atom.

Determining atomic positions by fitting each atom site using a spherical Gaussian algorithm in Matlab is a common method. For double-check of our conclusions, we used two different softwares: CalAtom [36, 37] and StatSTEM [38] and compare their calculating results. The average value distribution of data using these two softwares are keeping an exact consistency. For example, for the Fe-Fe bond length of strong ladder at room temperature, CalAtom reveals that they are 2.71 Å and 2.55 Å; the StatSTEM reveals that they are 2.72 Å and 2.54 Å. Besides, each bond length acquired from atoms-position-determination software are based on the statistics value of about 300 data, thus they are statistically meaningful. Furthermore, multiple images were recorded for most of the data we exhibit. The multiple images were averaged in order to reduce noise and artifacts induced by possible random drifts of the sample. In the average procedure, the alignment of these images was done by minimizing the shift of an individual image relative to the averaged image using an iterative rigid alignment method. Another methods to measure the artifacts in STEM images is to determine the displacements of atoms in which no off-center displacements would happen [39]. On the basis of this method, Lu, L. *et al.* measured the STO layers [39] with rms=4.8 pm, we observed the STO layers with rms=3.2 pm using CalAtom software.

Data availability. The datasets generated during the current study are available from the corresponding author on reasonable request.

References:

1. Pulvari, C. F. Ferrielectricity. *Phys. Rev.* **120**, 1670-1673 (1960).
2. Miller, R. C., Wood, E. A., Remeika, J. P. & Savage, A. Na(Nb_{1-x}V_x)O₃ system and "ferrielectricity". *J. Appl. Phys.* **33**, 1623-1630 (1962).

3. Scott, J. F. *et al.* Ferrielectricity in the metal-organic ferroelectric tris-sarcosine calcium chloride. *Phys. Rev. B* **95**, 094119 (2017).
4. Maisonneuve, V., Cajipe, V. B., Simon, A., Muhll, R. V. D. & Ravez, J. Ferrielectric ordering in lamellar CuInP₂S₆. *Phys. Rev. B* **56**, 10860-10868 (1997).
5. Liu, F. *et al.* Room-temperature ferroelectricity in CuInP₂S₆ ultrathin flakes. *Nat. Commun.* **7**, 12357 (2016).
6. Gou, G. & Rondinelli, J. M. Piezoelectricity across a strain-induced isosymmetric ferri-to-ferroelectric transition. *Adv. Mater. Inter.* **1**, 311-316 (2015).
7. Pitcher, M. J. *et al.* Tilt engineering of spontaneous polarization and magnetization above 300 K in a bulk layered perovskite. *Science* **347**, 420-424 (2015).
8. Spaldin, N. A., Fiebig, M. & Mostovoy, M. The toroidal moment in condensed-matter physics and its relation to the magnetoelectric effect. *J. Phys.: Condens. Matter* **20**, 2709-2713 (2008).
9. Oh, Y. S., Luo, X., Huang, F. T., Wang, Y. & Cheong, S. W. Experimental demonstration of hybrid improper ferroelectricity and the presence of abundant charged walls in (Ca,Sr)₃Ti₂O₇ crystals. *Nat. Mater.* **14**, 407-413 (2015).
10. Orlandi, F. *et al.* Structural and electric evidence of ferrielectric state in Pb₂MnWO₆ double perovskite system. *Inorg. Chem.* **453**, 10283-10290 (2015).
11. Dai, P., Hu, J. & Dagotto, E. Magnetism and its microscopic origin in iron-based high-temperature superconductors. *Nat. Phys.* **8**, 709-718 (2012).
12. Ying, J., Lei, H., Petrovic, C., Xiao, Y. & Struzhkin, V. V. Interplay of magnetism and superconductivity in the compressed Fe-ladder compound BaFe₂Se₃. *Phys. Rev. B* **95**, 241109 (R) (2017).
13. Zhang, Y., Lin, L. F., Zhang, J. J., Dagotto, E. & Dong, S. Sequential structural and antiferromagnetic transitions in BaFe₂Se₃ under pressure. *Phys. Rev. B* **97**, 045119 (2018).
14. Dong, S., Liu, J.-M. & Dagotto, E. BaFe₂Se₃: A high T_C magnetic multiferroic with large ferrielectric polarization. *Phys. Rev. Lett.* **113**, 187204 (2014).
15. Caron, J. M., Neilson, J. R., Miller, D. C., Llobet, A. & McQueen, T. M. Iron displacements and magnetoelastic coupling in the antiferromagnetic spin-ladder compound BaFe₂Se₃. *Phys. Rev. B* **84**, 180409 (R) (2011).

16. Svitlyk, V. *et al.* Crystal structure of BaFe₂Se₃ as a function of temperature and pressure: phase transition phenomena and high-order expansion of Landau potential. *J. Phys.: Condens. Matter* **25**, 315403 (2013).
17. Nambu, Y. *et al.* Block magnetism coupled with local distortion in the iron-based spin-ladder compound BaFe₂Se₃. *Phys. Rev. B* **85**, 064413 (2012).
18. Lei, H., Ryu, H., Frenkel, A.I. & Petrovic, C. Anisotropy in BaFe₂Se₃ single crystals with double chains of FeSe tetrahedra. *Phys. Rev. B* **84**, 214511 (2011).
19. Krztonmaziopa, A. *et al.* The synthesis, and crystal and magnetic structure of the iron selenide BaFe₂Se₃ with possible superconductivity at T_c = 11 K. *J. Phys.: Condens. Matter*, **23**, 402201 (2011).
20. Tian, H. *et al.* Interface-induced modulation of charge and polarization in thin film Fe₃O₄. *Adv. Mater.* **26**, 461-465 (2014).
21. Coey, M. Condensed-matter physics: charge-ordering in oxides. *Nature* **430**, 155-157 (2004).
22. Lin, L.-F. *et al.* Ferroelectric ferrimagnetic LiFe₂F₆: charge ordering mediated magnetoelectricity. *Phys. Rev. Mater.* **1**, 071401(R) (2017).
23. Caron, J. M. *et al.* Orbital-selective magnetism in the spin-ladder iron selenides Ba_{1-x}K_xFe₂Se₃. *Phys. Rev. B* **85**, 180405 (R) (2012).
24. Li, W., *et al.* Phase separation and magnetic order in K-doped iron selenide superconductor. *Nat. Phys.* **8**, 126-130 (2012).
25. Li, W., Dong, S., Fang, C., & Hu, J.-P. Block antiferromagnetism and checkerboard charge ordering in the alkali-doped iron selenides R_{1-x}Fe_{2-y}Se₂. *Phys. Rev. B* **85**, 100407 (R) (2012)
26. King-Smith, R. D., Vanderbilt, D. Theory of polarization of crystalline solids. *Phys. Rev. B* **47**, 1651-1654 (1993).
27. Aoyama, T., *et al.* Polar state induced by block-type lattice distortions in BaFe₂Se₃ with quasi-one-dimensional ladder structure. *Phys. Rev. B* **99**, 241109 (R) (2019).
28. Zheng, W., *et al.* Room temperature polar structure and multiferroicity in BaFe₂Se₃. *Phys. Rev. B* **101**, 020101 (R) (2020).
29. Hur, N. *et al.* Electric polarization reversal and memory in a multiferroic material induced by magnetic fields. *Nature* **429**, 392-395 (2004).

30. Leo, N. *et al.* Independent ferroelectric contributions and rare-earth-induced polarization reversal in multiferroic TbMn₂O₅. *Phys. Rev. B* **85**, 094408 (2012).
31. Lin, L.-F., Zhang, Y., Meoro, A., Dagotto, E. & Dong, S. Frustrated Dipole Order Induces Noncollinear Proper Ferrielectricity in Two Dimensions. *Phys. Rev. Lett.* **123**, 067601 (2019).
32. Kresse, G., J. Hafner. Ab initio molecular dynamics for liquid metals. *Phys. Rev. B* **47**, 558 (1993).
33. Kresse, G., Furthmüller, J. Efficient iterative schemes for ab initio total-energy calculations using a plane-wave basis set. *Phys. Rev. B* **54**, 11169-11186 (1996).
34. Perdew, J. P., Burke, K., Ernzerhof, M. Generalized gradient approximation made Simple. *Phys. Rev. Lett.* **77**, 3865 (1996).
35. King-Smith, R. D., Vanderbilt, D. Theory of polarization of crystalline solids. *Phys. Rev. B* **47**, 1651-1654 (1993).
36. Zhang, Q. *et al.* Multiple-ellipse fitting method to precisely measure the positions of atomic columns in a transmission electron microscope image. *Micron* **113**, 99-104 (2018).
37. Zhang, Q. *et al.* CalAtom: A software for quantitatively analysing atomic columns in a transmission electron microscope image. *Ultramicroscopy* **202**, 114-120 (2019).
38. De Backer, A., Van den Bos, K.H.W., Van den Bos, W., Sijbers, J., & Van Aert, S. StatSTEM: An efficient approach for accurate and precise model-based quantification of atomic resolution electron microscopy images. *Ultramicroscopy* **171**, 104-116 (2016).
39. Lu, L. *et al.* Topological defects with distinct dipole configurations in PbTiO₃/SrTiO₃ multilayer films. *Phys. Rev. Lett.* **120**, 177601 (2018).

Acknowledgments We acknowledge the National Natural Science Foundation of China (Grant Nos. 11834002, 11674055, and 11234011), National Key R&D Program of China 2017YFB0703100, and the 111 Project (Grant No. B16042). K.D. acknowledges the China Scholarship Council (CSC, No.201806320230) for sponsorship and 2019 Zhejiang University Academic Award for Outstanding Doctoral Candidates.. We thank Prof. Fang Lin for providing guidance on calculating atoms position and Dr. Andrew Studer for performing neutron powder diffraction. We thank Prof. Sang-Wook Cheong, Prof. Zhigao Sheng, Prof. Qianghua Wang, Prof. Meng Wang, Prof. Renkui Zheng, Prof. Takuya Aoyama, Dr. Zhibo Yan, and Dr. Meifeng

Liu for valuable discussion and/or technical help during measurements.

Author contributions H.T., S.D., Z.Z, and G.V.T. co-designed the project. K.D. performed the experiments related to electron microscopy. K.D. and X.C. conduct the in-situ heating experiments. K.D. and Z.N.Z. designed the displacement vector-mapping algorithm for the statistics of bond length. L.G. and Y.L. synthesized the samples. L.G., J.P., Y.L., T.Z., J.L., and Z.N. measured macroscopic physical properties. Y.Z. and S.D. did DFT calculations. S.D. figured out the Landau theory formula. S.D., J.P., and S.S.W. analyzed the symmetry. K.D., S.D., H.T., and G.V.T. co-write the paper. All authors contributed to the discussions and manuscript preparation. K.D., L.G., and J.P. contributed equally.

Competing interests The authors declare no competing interests.

Author Information Reprints and permissions information is available at www.nature.com/reprints. Readers are welcome to comment on the online version of the paper. Correspondence and requests for materials should be addressed to H.T. (hetian@zju.edu.cn) and S.D. (sdong@seu.edu.cn).

1 Supplementary Information for

2 **Direct Visualization of Irreducible Ferrielectricity in Crystals**

3 Kai Du^{1#}, Lei Guo^{2#}, Jin Peng^{2#}, Xing Chen¹, Zheng-Nan Zhou¹, Yang Zhang², Ting Zheng²,
4 Yan-Ping Liang², Jun-Peng Lu², Zhen-Hua Ni², Shan-Shan Wang², Gustaaf Van Tendeloo^{3,4}, Ze
5 Zhang¹, Shuai Dong^{2*}, He Tian^{1*}

6 ¹Center of Electron Microscopy, State Key Laboratory of Silicon Materials, and School of
7 Materials Science and Engineering, Zhejiang University, Hangzhou, 310027, China

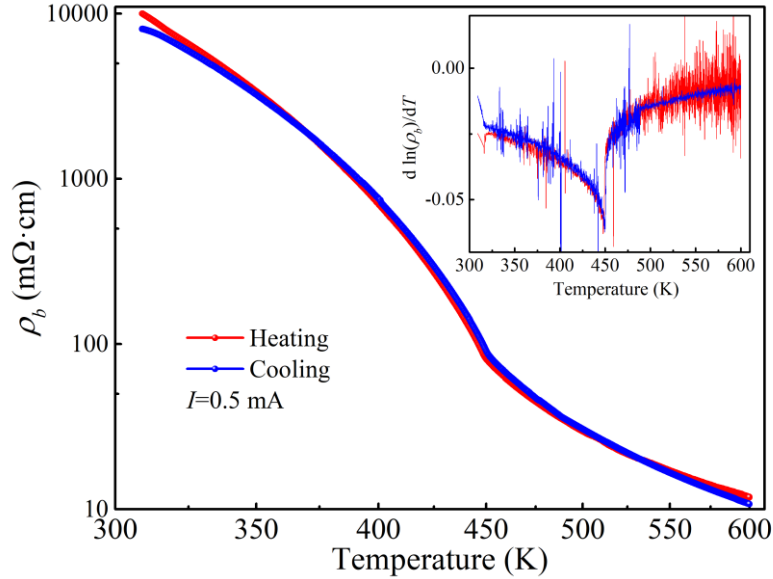
8 ²School of Physics, Southeast University, Nanjing 211189, China

9 ³Electron Microscopy for Materials Science (EMAT), University of Antwerp, Groenenborgerlaan
10 171, B-2020 Antwerp, Belgium

11 ⁴Nanostructure Research Centre (NRC), Wuhan University of Technology, Wuhan, 430070,
12 China

13 [#]These authors contributed equally.

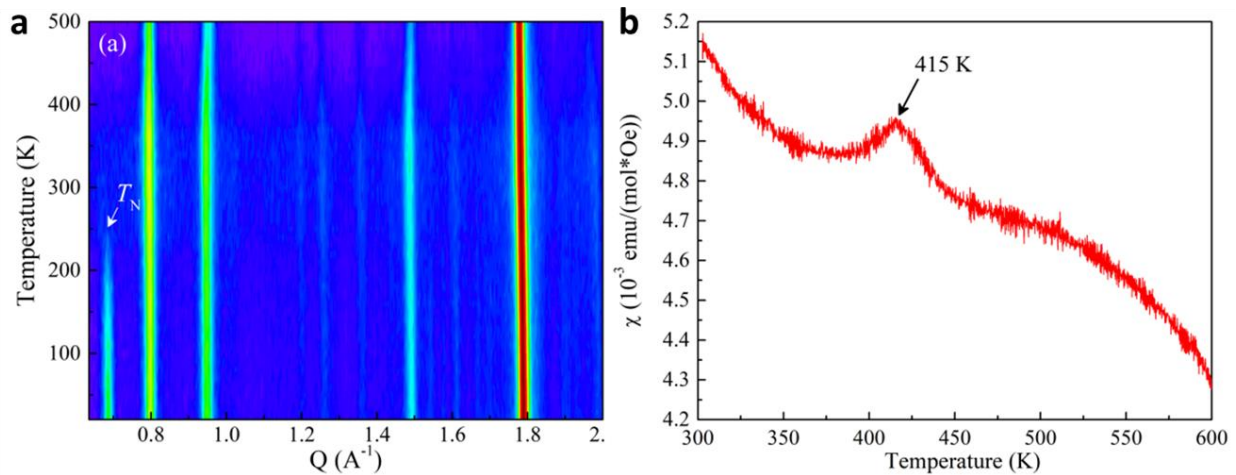
14 ^{*}Correspondence to: Email: hetian@zju.edu.cn; sdong@seu.edu.cn;



15

16 **Supplementary Figure 1** Temperature dependence of the resistivity (ρ_b). Insert: the derivative of
 17 $\ln(\rho_b)$. The resistivity changes its behavior near 450 K, which also supports the scenario of a first-
 18 order transition. The measuring current is along the b-axis. Noting this material is highly
 19 conductive (although it is not a metal) with a very small experimental band gap (e.g. 0.178 eV or
 20 0.13 eV) [17, 18], it is technically challenging to directly measure its small polarization (~ 0.1
 21 $\mu\text{C}/\text{cm}^2$) hysteresis loop, i.e. to demonstrate the switching of polarization. Noting that the anomaly
 22 of resistivity occurs at a little higher temperature than T_{C2} of DSC ($\sim 417\text{-}425$ K) for the following
 23 possible reasons. First, usually thermometers for different experiments are not well relatively-
 24 calibrated, especially for the high-temperature range. Second, maybe for such a first order
 25 transition, resistivity always changes at a little higher temperature, according to the SHG result of
 26 Ref. [27].

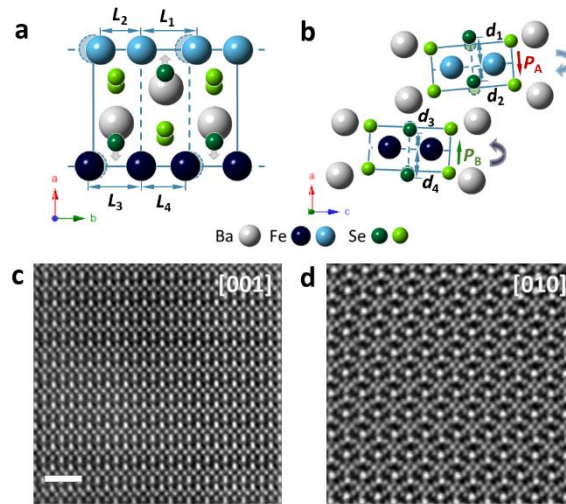
27



28 **Supplementary Figure 2** Macroscopic physical properties. (a) Contour plot of the neutron powder
 29 diffraction spectrum, collected on the high-intensity powder diffractometer WOMBAT at the
 30 Australian Nuclear Science and Technology Organisation (ANSTO) with $\lambda = 2.41 \text{ \AA}$, between 10
 31 K and 500 K. The magnetic peak at $Q = 0.7 \text{ \AA}^{-1}$ for block-type antiferromagnetism appears below
 32 $\sim 250 \text{ K}$, in agreement with literature. No other long-range magnetic order is observed in the whole
 33 spectrum from $Q = 0.63 - 4.75 \text{ \AA}^{-1}$. (b) Magnetic susceptibility peaked at $\sim 415 \text{ K}$, measured under 1
 34 T field. Neutron powder diffraction confirms the appearance of long range magnetic ordering
 35 below $\sim 250 \text{ K}$, in agreement with previous report of ($\sim 255 \text{ K}$) [17, 18] and ($\sim 256 \text{ K}$) [15]. Thus,
 36 the peak of the magnetic susceptibility at $\sim 415 \text{ K}$ (appearing only under strong magnetic field, e.g.
 37 $\sim 1 \text{ T}$) should be a side effect of a polar structural transition, instead of a magnetic phase transition.

38

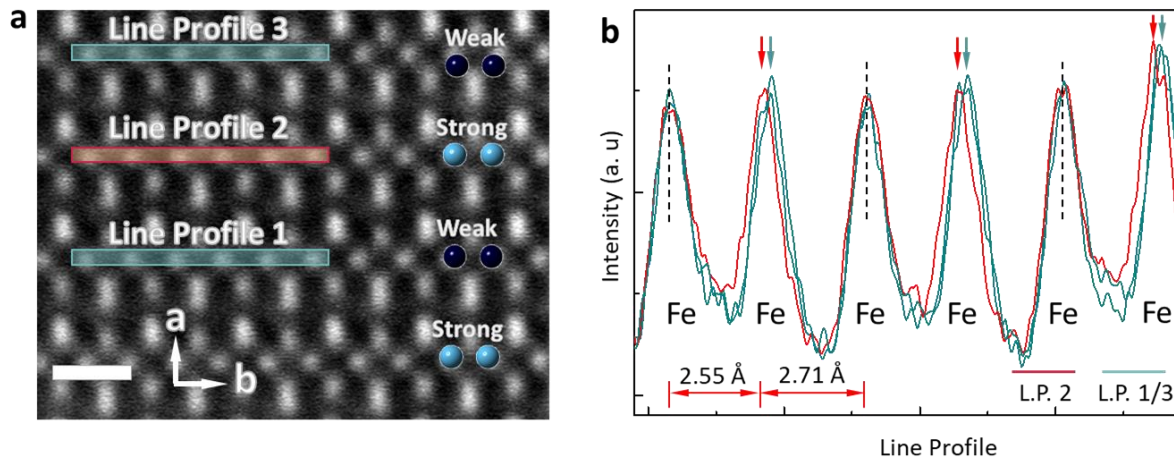
39



40

41 **Supplementary Figure 3** STEM images and sketches of BaFe_2Se_3 along (a) and (c) the $[001]$
 42 direction, (b) and (d) $[010]$ direction. BaFe_2Se_3 , having an orthorhombic crystal structure, was
 43 analyzed with different temperature and external bias. Samples were cut into lamellas with the
 44 widest faces perpendicular to the crystal principal axis ($[010]$ and $[001]$) by Focused Ion Beam for
 45 the observation in the electron microscope. Since the BaFe_2Se_3 is easily dissociated along the $[100]$
 46 plane which could be observed easily, it is convenient to judge orientation and perform further
 47 analysis of the accurate crystal structure on the basis of HAADF images along a target direction.
 48 Scale bar, 1 nm.

49



50

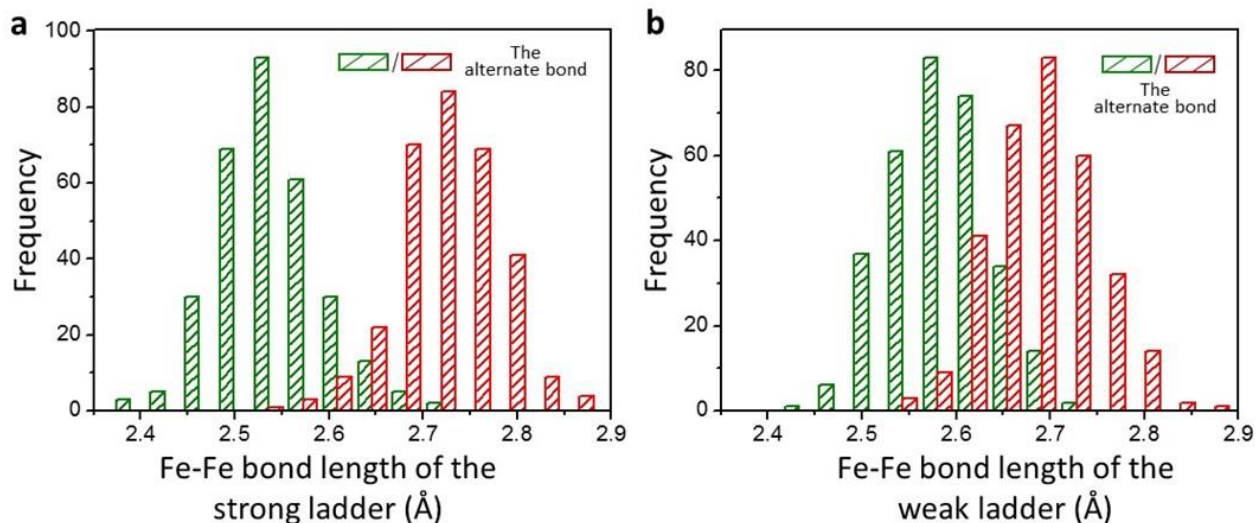
51 **Supplementary Figure 4** STEM image of BaFe_2Se_3 along the c -axis and corresponding line

52 profiles. (a) HAADF-STEM images along the c -axis. (b) Corresponding line profiles which are

53 extracted from the red and cyan boxes in (a), which represent weak and strong ladders respectively.

54 The difference between the bond length of strong and weak ladders is clearly observed. Scale bar,

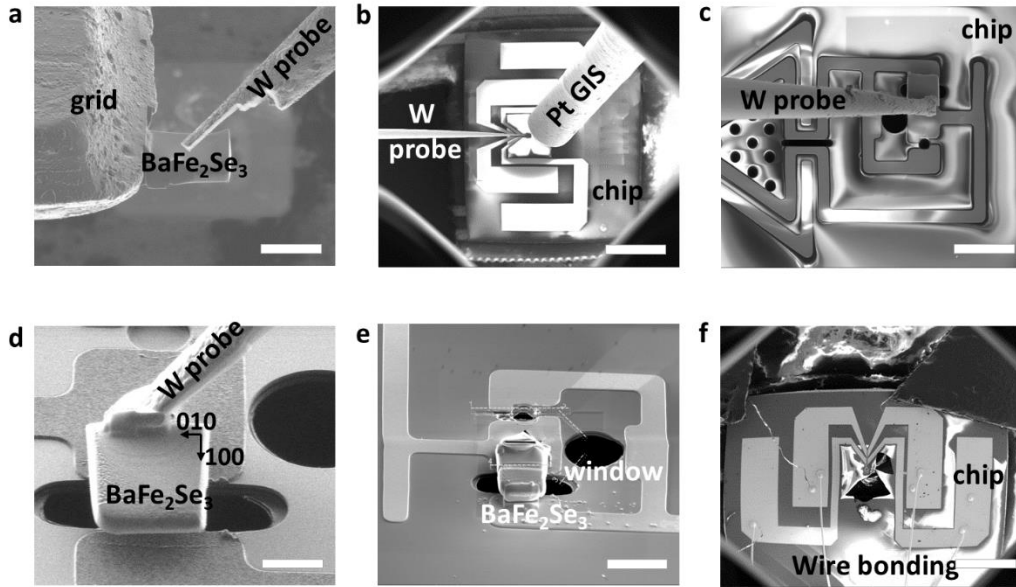
55 5 Å.



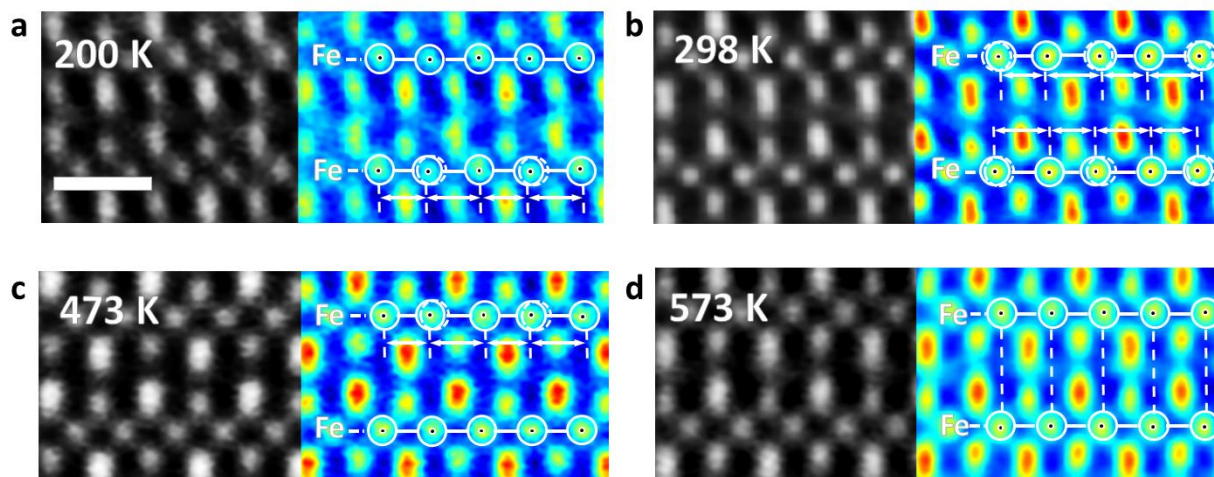
56 **Supplementary Figure 5** Measurement of the displacements. Based on the statistics of about 300
 57 data, Fe-Fe bond lengths of the (a) strong ladder and (b) weak ladder are shown. According to the
 58 most probable values of distributions, the alternate Fe-Fe bond lengths in strong ladders are
 59 2.55 ± 0.04 Å and 2.71 ± 0.04 Å respectively, in which the displacement of Fe atoms are stronger
 60 than that in the weak ladders where the Fe-Fe bond lengths reach 2.69 ± 0.04 Å and 2.57 ± 0.03 Å
 61 respectively. Strickly speaking, there are eight kinds of the Fe-Fe distance in the leg direction,
 62 since in the $Pmn2_1$ space group the Fe-Fe rectangles are already slightly distorted to be trapezoidal.
 63 However, these trapezoidal distortion is very weak (~ 0.013 Å according to Ref. [27]), while the
 64 tetramerization distortion is in the range of 0.05-0.25 Å according to our STEM data. Due to the
 65 resolution limit of STEM, these eight kinds of the Fe-Fe distance degenerate as four kinds, by
 66 neglecting the tiny trapezoidal distortion.

67

68



69 **Supplementary Figure 6** The SEM images showing the technique using a probe in order to put
 70 the sample onto a chip for testing the macroscopic properties tests. Some tests including the
 71 ferroelectric measurements along the a -axis and its behavior with temperature are done on these
 72 micro devices. (a) Welding the sample to tungsten probe (marked as W probe) and cutting the
 73 sample from the grid. Scale bar, 10 μm . (b) Transfer of the sample to the four-probe electricity
 74 chip and welding it onto the chip by Pt GIS. Scale bar, 1 mm. (c) Enlarged view of the end region
 75 of the chip. We place the chip on the window between electrodes which act as heat conductor or
 76 electric conductor. Scale bar, 15 μm . (d) Magnified image of the end region. Scale bar, 3 μm . (e)
 77 Polishing the surrounding area of the lamella by a Ga ions beam. Scale bar, 10 μm . (f) Connecting
 78 useful electrodes to external equipment by wire-bonding. Scale bar, 0.3 mm.

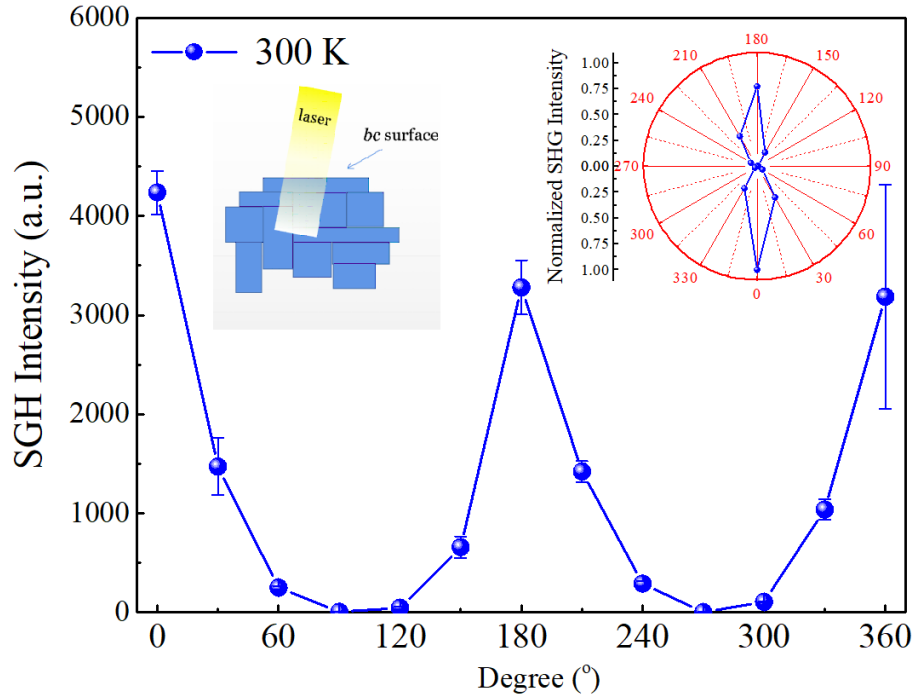


79

80 **Supplementary Figure 7** Color-enhanced HAADF-STEM images acquired at different
 81 temperatures along the *c*-axis. The strong ladder shows distinct tetramerization at (a) 200 K, (b)
 82 298 K, and (c) 473 K, and the weak ladder reveals tetramerization at (b) 298 K. The difference of
 83 Fe-Fe bond length at high temperature (d) 573 K vanishes in both ladders indicating that in-ladder
 84 tetramerization almost drops to zero. Scale bar, 5 Å.

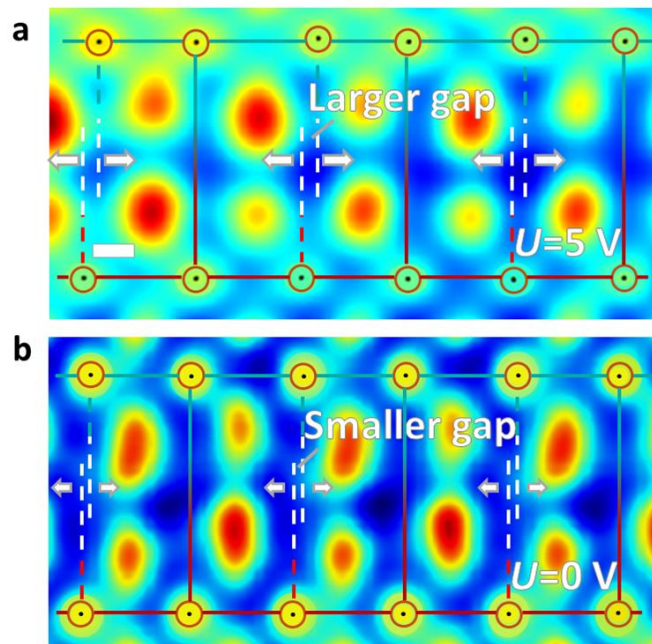
85

86

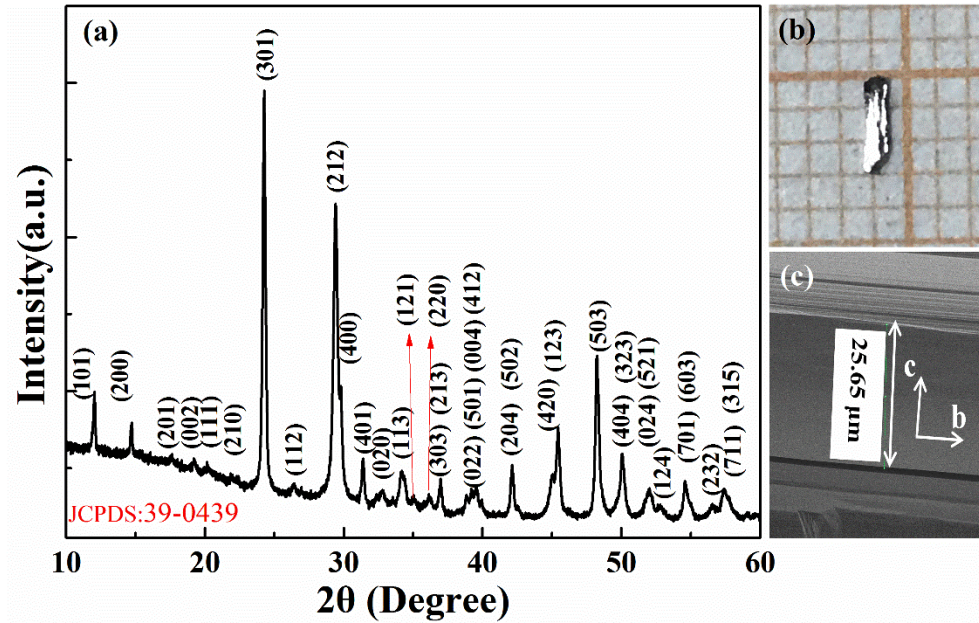


87

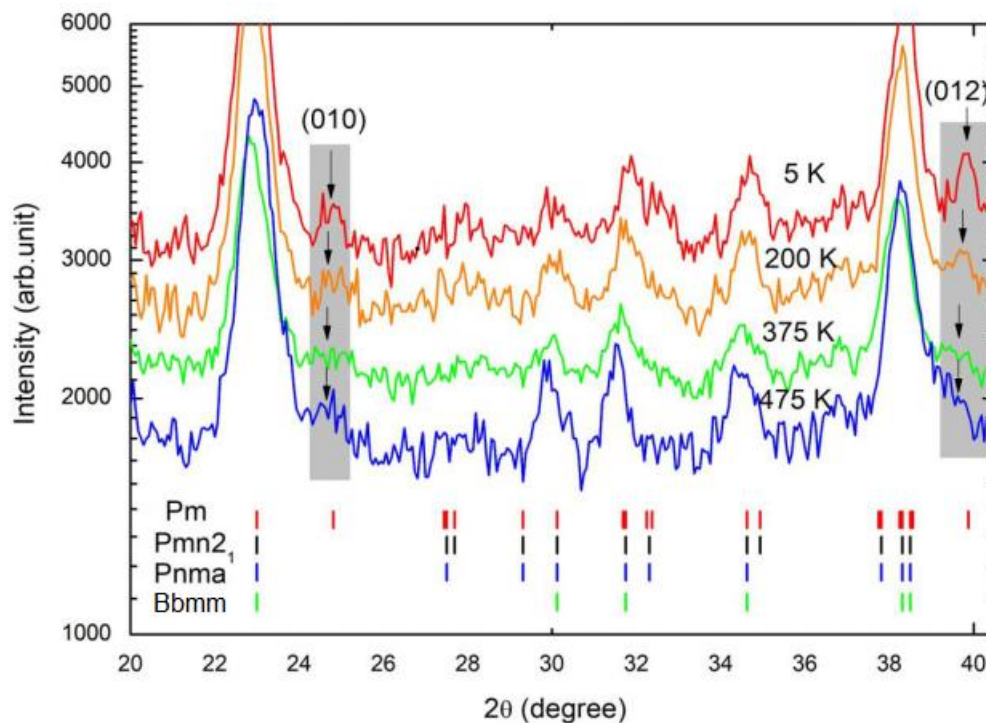
88 **Supplementary Figure 8** In-plane rotation of the polarization direction of the incident laser. The
 89 initial polarization (i.e. electric field component E) of the incident laser is along the c -axis. Insert
 90 (right): a polar diagram. A single axis behavior, i.e. 180° as a period, is evidenced. We repeated
 91 such rotation in several temperatures, and the 180° symmetry did not change. When $E \parallel b$, the signal
 92 is almost zero, which can exclude the surface contribution. Although our crystal only own large
 93 cleavage surface of bc plane [see Fig. S10b], the laser of 800 nm wavelength used in SHG
 94 measurement can penetrate into the crystals partially and reflects some ‘inner’ information beyond
 95 the surface, as sketched in insert (left). In fact, the SHG measurements can even create small
 96 burning holes by light spots. Then the P_a contribution from inner twin crystals are very possible to
 97 be detected by SHG. Considering the much larger amplitude of P_a than P_c (in most cases $P_a \sim 10$ -
 98 $100P_c$), a little concentration of P_a domain can dominant the SHG signal, over the P_c ’s signal.
 99 Another source of P_a ’s signal is the canting angle of incident laser. If the incident angle is not
 100 exactly perpendicular to the bc surface, the electric field component along the a -axis will be
 101 available.



102 **Supplementary Figure 9** Color-enhanced HAADF-STEM images of the difference of Fe atoms
 103 displacement in the in-situ bias experiment. The neighboring Fe-Fe bond length in the weak chain
 104 under bias is equal while an enhanced tetramerization of the Fe-block is observed on the strong
 105 chain. The difference between weak and strong chain evolution is much smaller without bias. The
 106 enhanced tetramerization here indicates a corresponding enhanced polarization along the a -axis.
 107 Scale bar, 1 Å.



108 **Supplementary Figure 10** (a) X-ray powder diffraction of BaFe₂Se₃. Optical (b) and SEM (c)
 109 microscopy on BaFe₂Se₃ fiber show that the extension direction is actually along *b*-axis, thus the
 110 direction of Fe chains. Each piece of our sample (of mm size) is consisted of many loosely-
 111 contacted tiny needle-like crystals. For these crystals, the needle direction is along the *b*-axis, while
 112 the typical scale of crystals along *a*- or *c*-axis is only of μm size. Only relative large (still very
 113 small) *bc* cleavage surface is available, and it does not imply a whole single crystalline below the
 114 surface. Twin crystals are very possible below the cleavage surface (see insert of Fig. S8),
 115 considering the edge with chipped steps besides the very small cleavage surface (see the SEM
 116 image).



117

118 **Supplementary Figure 11** Magnified view of neutron powder diffraction of BaFe₂Se₃. The

119 indexes of possible space groups (No. 63 *Bbmm*, No. 62 *Pnma*, No. 31 *Pmn2₁*, and No. 6 *Pm*) are

120 marked. Our result supports the *Pm* space group from 475 K to 5 K. The two characteristic peaks

121 of *Pm* space group are highlighted, which are forbidden in the *Pmn2₁* and *Pnma* space groups.

122 Noting that our neutron diffraction pattern are generally in agreement with previous measurements

123 [15, 17]. The two weak peaks which are allowed in the low symmetry space group but forbidden

124 in the high symmetry one are close to the precision limit of our neutron spectrometer. In fact, the

125 powder neutron diffraction data can be well refined with either the *Pm*, *Pmn2₁* or *Pnma* space

126 group, as done in previous works. In short, for this material, it's hard to distinguish these space

127 groups with neutron data only, but the neutron data can be a supplementary support to our STEM

128 data.

129

130

131

132 **Supplementary Table 1** Statistics of the deviation of Fe-Fe bond length in the strong and weak
133 chain at different temperatures. The standard deviation and standard error are colored by green
134 and yellow, respectively.

T (K)	Δ Strong Chain (Å)	Δ Weak Chain (Å)
200	$0.18 \pm 0.06(0.004)$	$0.03 \pm 0.08(0.005)$
240	$0.15 \pm 0.05(0.003)$	$0.07 \pm 0.05(0.003)$
270	$0.15 \pm 0.03(0.002)$	$0.08 \pm 0.04(0.002)$
298	$0.16 \pm 0.04(0.002)$	$0.12 \pm 0.04(0.002)$
343	$0.19 \pm 0.05(0.003)$	$0.16 \pm 0.06(0.004)$
373	$0.20 \pm 0.04(0.002)$	$0.18 \pm 0.05(0.003)$
423	$0.24 \pm 0.03(0.002)$	$0.07 \pm 0.03(0.002)$
473	$0.17 \pm 0.05(0.002)$	$0.01 \pm 0.05(0.003)$
573	$0.01 \pm 0.04(0.002)$	$0.01 \pm 0.05(0.003)$

Deviation of Bond length \pm standard deviations (standard errors)

135